

**Physical Experimentation and Actuated Wheel
Design for Granular Locomotion Using Resistive
Force Theory**

by

David Carrington Motley

Submitted to the Department of Mechanical Engineering
in partial fulfillment of the requirements for the degree of

Bachelor of Science in Mechanical Engineering

at the

MASSACHUSETTS INSTITUTE OF TECHNOLOGY

June 2016

© Massachusetts Institute of Technology 2016. All rights reserved.

Signature redacted

Author

Department of Mechanical Engineering

May 13, 2016

Signature redacted

Certified by

Ken Kamrin

Assistant Professor of Mechanical Engineering

Thesis Supervisor

Signature redacted

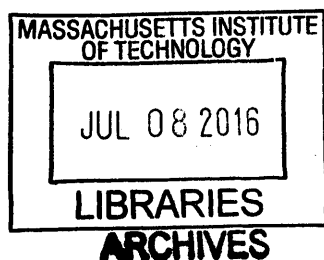
Accepted by ...

.....

Anette Hosoi

Associate Professor of Mechanical Engineering

Undergraduate Officer



Physical Experimentation and Actuated Wheel Design for Granular Locomotion Using Resistive Force Theory

by

David Carrington Motley

Submitted to the Department of Mechanical Engineering
on May 13, 2016, in partial fulfillment of the
requirements for the degree of
Bachelor of Science in Mechanical Engineering

Abstract

Physical experiments were conducted using 3D printed wheels and a sand testing bed to explore the applications and predictive power of the Resistive Force Theory (RFT), an empirical model based on linear superposition designed to predict the interactive forces between solid bodies and granular media. Four-spoke wheel designs, made of four treads with a hinge halfway down each tread set to a prescribed angle θ , and cylindrical wheels were used to validate a scaling law determined from RFT. The 3D printed wheels were attached to an experimental test rig that consisted of a motor fixed to a carriage free to move horizontally and vertically. Data was gathered through a series of horizontal, vertical, and angular position sensors and a set of force and torque sensors, then processed with a MATLAB script and determined to validate the RFT scaling law.

Next, the design of an actuated wheel capable of altering its shape while in motion was explored. RFT predicts that as motion conditions of the wheel change, a corresponding change in the shape of the wheel would lead to an improvement in the wheel's performance. In order to properly analyze the effect of the change of shape of the wheel, the actuated wheel was designed to first only change shape in the in-plane dimension, and second be sufficiently rigid such that it does not exhibit excessive deformation in the new shape while under load. Several designs were explored, and the final form of the "FrankenWheel" is designed with a series of five flaps that rotate to fixed angles using a system of gears, hinges, and a secondary motor. This version of the "FrankenWheel" has been assembled for testing.

Thesis Supervisor: Ken Kamrin

Title: Assistant Professor of Mechanical Engineering

Acknowledgments

I would like to thank several people who have helped me throughout the course of this multi-year research project starting with Professor Ken Kamrin. I am so grateful that he asked me to join his research team my sophomore fall. He has been an invaluable research PI and advisor. Without him this project would have been nigh impossible, and I have truly enjoyed the past two and a half years I have spent working with him.

I would also like to thank James Slonaker. He too has been instrumental in working on this project, working with me side by side in the lab for almost the entirety of this project. His input and experience helped in gathering data in the lab and in making the many design decisions necessary to build the actuated wheel. It was an absolute pleasure to get to know him while working on this project.

Next I would like to thank Carmine Senatore. Thank you to Carmine for designing and building the experimental test rig that was used throughout the course of the project. I really appreciate you taking the time to introduce to all of the equipment and software used in operating the rig. Finally I want to thank Professor Karl Iagnemma for offering us his lab space to use for our experiments. Access to a lab space that aligned so well with what we wanted to test was extremely helpful.

Contents

1	Introduction	13
2	Background	17
2.1	MATLAB Simulation and Optimization	17
2.2	Fundamental Scaling Law	20
3	Physical Experiment Design	23
3.1	3D Printing of Wheels	23
3.2	Sand Test Bed Setup	29
3.3	Data Collection and Analysis Methods	32
4	FrankenWheel Design	37
4.1	Superball Design	38
4.1.1	Design and Actuation	39
4.2	FrankenWheel 2.0	43
4.2.1	Ideation and Decisions	44
4.2.2	Actuation Method	46
4.2.3	Central Hub and Flaps	53
4.2.4	Motor and Motor Mount	57
4.2.5	Production and Final Assembly	60
4.3	Further Experimentation	62
A	Data Analysis Code	65
A.1	Data Visualization Code	65

A.2 Steady State Averages Calculation Code 68

List of Figures

1-1	General four-spoke design.	14
2-1	Velocity and Power contour plots [3].	18
2-2	Velocity contour plot overlain with Power contour plot [3].	19
2-3	Maximum velocity and power wheel designs [3]	20
3-1	Initial four-spoke wheel design.	24
3-2	Cross pieces along with cylindrical clamp that together were used to couple four-spoke wheels to the motor output shaft.	25
3-3	Four-spoke wheel design with cross piece cutaway shown from multiple perspectives.	26
3-4	Makerbot Replicator 2 Desktop 3D Printer [1].	27
3-5	A pair of four-spoke wheels used in testing.	28
3-6	3D printed cylindrical wheels.	29
3-7	Sand test bed setup	31
4-1	"Superball" shapes for different χ values.	39
4-2	Multiple views of rigid skeleton design for the superball shape family.	40
4-3	Drawing of four-bag rubber-spring steel interface design.	41
4-4	Sliding contact design.	42
4-5	Universal bag design.	43
4-6	Potential actuated wheel design ideas.	45
4-7	Four-flanged cylinder concept.	47
4-8	String-motor design.	48

4-9 Pulley-motor design.	48
4-10 Piston actuated design.	49
4-11 Pneumatically actuated balloon design.	50
4-12 New gear train design.	51
4-13 Small and Large Gears.	53
4-14 SolidWorks image of central hub.	54
4-15 3D printed central hub.	55
4-16 SolidWorks image of flap with Shatfloc coupling mechanism.	56
4-17 Flap design with set screw coupling mechanism.	57
4-18 Motor mount.	59
4-19 SolidWorks image of parts to be assembled for FrankenWheel.	60
4-20 Multiple views of the assembled FrankenWheel.	62

List of Tables

- 3.1 Cylindrical Wheel Inputs [3] 29
- 4.1 Gantt Chart of Rotation vs. Extension 46

Chapter 1

Introduction

The field of Fluid Mechanics is centuries old, and as such much of the behavior and interactions between solid and fluid bodies are well defined. Countless years of study have yielded equations and scaling relationships to be derived that provide an intimate knowledge of the interactions between solid and fluid bodies. Powerful equations, such as Navier-Stokes, allow the various interaction forces to be solved for as a body, such as a plane or a boat, move through a fluid. Scaling relationships, such as the Reynolds number, allow for relatively straightforward modeling and testing of either large scale or small scale objects.

However, the study of the interaction of bodies with granular media, such as sand, snow, dirt, and gravel is a very young field, and as such the knowledge of the field is limited in comparison with that of fluids. The behavior of granular media is further complicated by the fact that they behave like both solids and fluids, as they are rigid like a solid until their yield stress is exceeded at which point they flow like a fluid. Modeling the interaction of solid bodies with granular materials, while possible, is usually quite complex and computationally intensive. Resistive Force Theory (RFT) as applied to granular locomotion, developed by Chen Li et. al, has the potential to change this [2]. This theory is based on a relatively simplistic model, which was developed to model the interaction between rigid bodies and non-cohesive granular materials, and originally simulated animal locomotion [2]. Since then the application of Resistive Force Theory has been expanded to simulate, predict, and

optimize the wheel design for vehicles moving through granular material [3]. Resistive Force Theory was also used to derive a set of fundamental scaling laws governing the interaction between rigid bodies and granular media [3]. Resistive Force Theory drastically reduces the time needed to simulate the interactions between rigid bodies and granular media.

Physical experiments were needed to validate the expanded applications of RFT. Initially physical experiments were conducted using cylindrical wheels of the same shape but scaled to different sizes to test the validity of the previously derived fundamental scaling laws. Next different variations of a four-spoke wheel design, made of four identical treads with a hinge halfway down each tread set to a prescribed angle θ . Figure 1-1 shows a representative four-spoke wheel design.

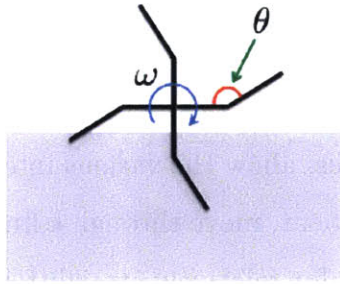


Figure 1-1: General four-spoke design.

Four-spoke wheels, each with a different prescribed angle θ were used to further test the predictive powers of the granular locomotion simulation based on RFT. Finally after conducting the previous tests to validate RFT's expanded applications, a self-actuating wheel, capable of changing its shape while in motion, was designed and built.

Chapter 2 defines the MATLAB simulation designed to apply RFT to granular locomotion as well as the optimization routines utilized therein, and also explains the derivation and functional form of the scaling laws derived from RFT. Chapter 3 describes the processes used to create the four-spoke and cylindrical wheels used in testing, and details the nature of the physical experiments, including the sand test

bed setup and apparatus used in testing, as well as the method of data collection and analysis. Chapter 4 describes the design process for the self-actuating wheel.

Chapter 2

Background

As mentioned in Chapter 1, Resistive Force Theory was originally designed to simulate animal locomotion in granular materials, however it has since been used to simulate wheeled locomotion in granular materials as well as to derive a set of fundamental scaling laws. The nature of these two expanded applications are discussed below.

2.1 MATLAB Simulation and Optimization

A MATLAB simulation used for optimization of vehicular granular locomotion was created by James Slonaker. Before the simulation was created the scalable stress profiles, that detail the various forces acting on a plate at various angles of attack and angles of intrusion, were expanded to include the full 360° range of angles of intrusion [3]. The original RFT model used a limited 180° range for simplicity [2]. Then a simulation was created which integrates the equations of motion to simulate the rotation and translation of the wheel. The simulation uses the rotation matrix to track the relative position and velocity of various spokes of the wheel, and a combination of RFT, which through linear superposition along discrete segments predicts the net force and torque acting on the wheel, and Newton's Second Law to calculate accelerations [3]. The simulation assumes that wheel is rotating by itself without being attached to a vehicle.

The simulation then requires several inputs including the tire mass, fixed rotation speed, initial position and velocity of the wheel, the gravitational acceleration, and if wanted a drawback force. It also requires the following parameters regarding the wheel design: the characteristic length, the width of the wheel in the plane, and a single parameter designating the shape of the wheel. The simulation then outputs an array of velocities, positions, and energies dissipated for each simulated time step [3]. Initially the movement of the wheel is characterized by a transient state of dynamic movement, but eventually it settles into an oscillatory steady state path with a constant period and amplitude [3]. The simulation also outputs an average steady state velocity and power expended computed over an arbitrarily chosen steady state period [3].

When attempting to optimize wheel design, the steady state velocity of the wheel and the steady state power expended were used as performance metrics. Optimal wheel performance was defined to be achieving the maximum average steady state velocity for the minimum average power expended. Average velocity and power contour plots were generated as wheels were simulated over a range of rotational velocities and a range of hinge angles with the other inputs fixed. Sample contour plots for x-direction velocity and power are provided in Figure 2-1.

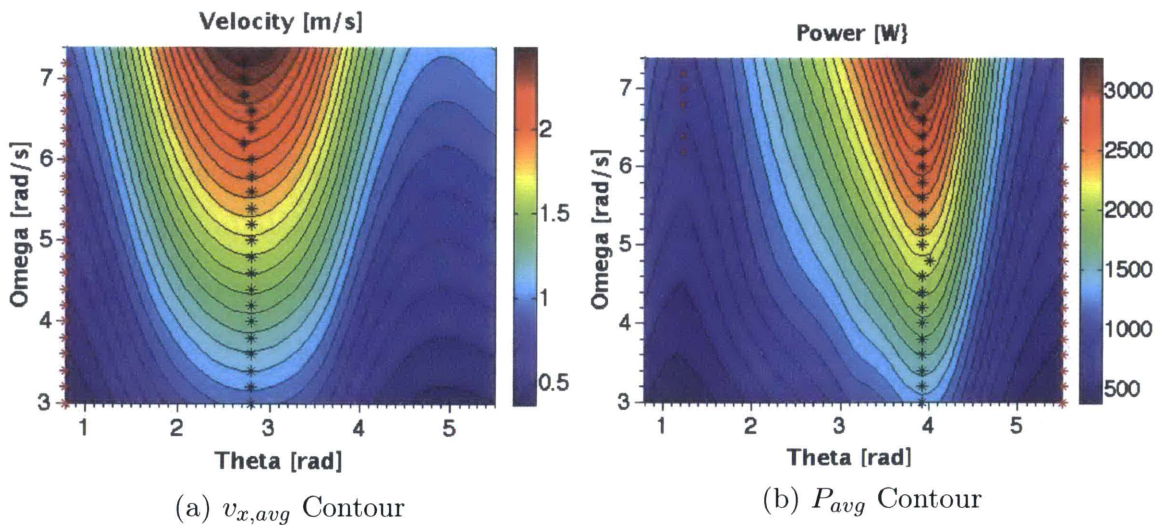


Figure 2-1: Velocity and Power contour plots [3].

Then to determine which hinge angle minimizes power expended for a given average velocity, standard minimization techniques were used [3]. Optima, i.e. a minimum, defined to be local points where the gradients of the velocity and power contours are parallel, were computed in the simulation by taking the cross product of the two gradients [3]. When this cross product was approximately zero it was considered to be a point of tangency [3]. Then the velocity contour plot was overlain with the power contour plot, and the points at which the velocity contour plot is parallel to the power contour plot indicate the optimum hinge angle[3]. A sample plot of optimum angles is shown below in Figure 2-2.

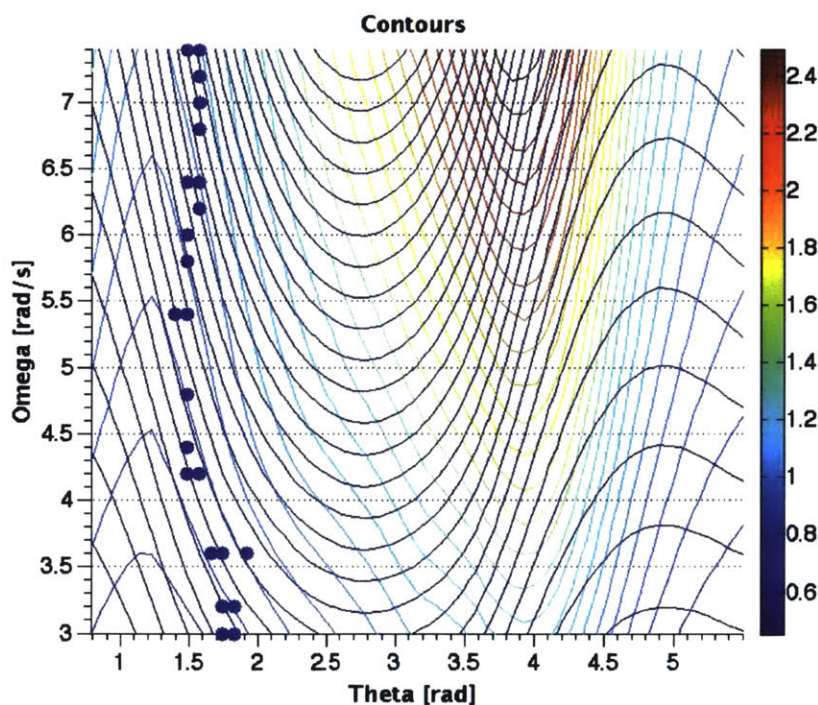


Figure 2-2: Velocity contour plot overlain with Power contour plot [3].

Next another series of simulations was run to see if varying the characteristic length or mass of the wheel had any effect on the hinge angle that produced the highest average velocity, and the highest maximum power expended respectively. Note that the hinge angle producing the highest average power expended is the worst design as it expends more power than all other designs keeping all other experimental parameters constant. For these simulations velocity and power contour plots were

generated for a series of discrete characteristic lengths or masses of the wheel. Overall Slonaker's results indicated that changes in characteristic length or mass of the wheel had a small effect on the hinge angle that produced the maximum velocity and maximum power expended. The simulations demonstrated that optimum hinge angles, producing the maximum velocity, occurred at $\theta < 180^\circ$, and the least optimum hinge angle, producing the maximum power expended, occurred $\theta > 180^\circ$ [3]. A visual of these designs assumed to be rotating clockwise is shown in Figure 2-3 below.

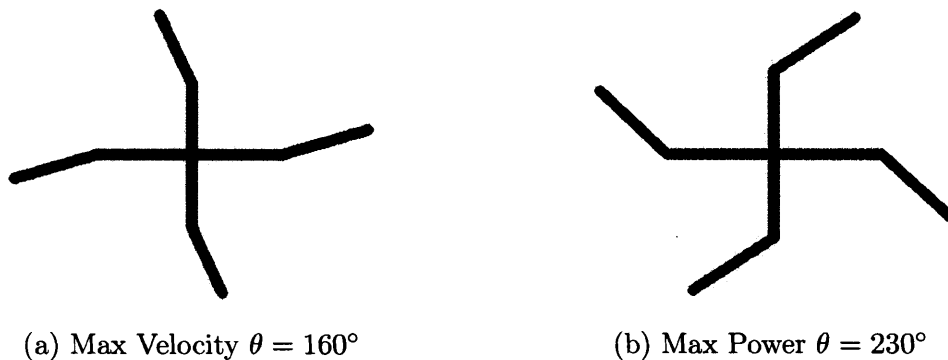


Figure 2-3: Maximum velocity and power wheel designs [3]

2.2 Fundamental Scaling Law

The existence of a global scaling law was then postulated based on the prior simulation results and the simplicity of the RFT model [3]. Slonaker defined the system inputs for an arbitrarily shaped wheel rotating freely which were similar to what was used in the simulation. The inputs include a wheel boundary, defined by the polar set $r = Lf(\theta)$, where L is the characteristic wheel length and f the function which prescribes the shape of the wheel, a mass m , a constant wheel velocity ω , an out of plane dimension D , a gravitational acceleration g , and a drawback force F_{draw} acting on the shaft [3]. The type of granular material the wheel is moving through is also an input and is controlled for by a scaling parameter ζ derived from RFT [3]. Note, however, that this scaling parameter can be further defined using Plasticity theory to be a function of the density of the sand ρ , the gravitational acceleration g ,

the coefficient of friction of the sand μ , and the coefficient of sand material interface μ_w [3]. The average velocity and average power can thus be written as functions ψ_v and ψ_p of these inputs as seen in equations 2.1 and 2.2 below.

$$v_{avg} = \psi_v(\omega, L, f, m, g, F_{draw}, \zeta(\mu, \mu_w)) \quad (2.1)$$

$$P_{avg} = \psi_p(\omega, L, f, m, g, F_{draw}, \zeta(\mu, \mu_w)) \quad (2.2)$$

Next dimensional analysis was performed using L as the characteristic length, m as the characteristic mass, and $\frac{1}{\omega}$ as the characteristic time [3]. The non-dimensional groups are defined by the following equations 2.3, 2.4, and 2.5.

$$\tilde{g} = \frac{g}{L\omega^2} \quad (2.3)$$

$$F_{draw}^{\tilde{}} = \frac{mg}{F_{draw}} \quad (2.4)$$

$$\tilde{\zeta}D = \frac{\rho\hat{\zeta}(\mu, \mu_w)DL^2}{m} \quad (2.5)$$

Note that $\hat{\zeta}$ is the non-dimensional form of ζ . Using the above non-dimensional groups, global scaling relationships were derived as seen in equation 2.6 and 2.7 below.

$$v_{avg} = L\omega\tilde{\psi}_v\left(f, \frac{g}{L\omega^2}, \frac{mg}{F_{draw}}, \frac{\rho\hat{\zeta}(\mu, \mu_w)DL^2}{m}\right) \quad (2.6)$$

$$P_{avg} = mL^2\omega^3\tilde{\psi}_p\left(f, \frac{g}{L\omega^2}, \frac{mg}{F_{draw}}, \frac{\rho\hat{\zeta}(\mu, \mu_w)DL^2}{m}\right) \quad (2.7)$$

Subsequently, a functional scaling law was derived from equations 2.6 and 2.7 above. Note for simplicity that the wheel shape and the type of sand are assumed constant, meaning the wheel shape function (f), the RFT scaling parameter ($\hat{\zeta}(\mu, \mu_w)$), and the sand density (ρ) are constant. Thus the system has three degrees of freedom, but six non-constant parameters including ω , L , m , g , F_{draw} , and D . Thus three

scaling factors A , B , and C were chosen and are defined in equation 2.8.

$$\bar{g} = Ag, \bar{L} = BL, \bar{m} = Cm \quad (2.8)$$

Then the other three non-constant parameters ω , F_{draw} , and D were written in terms of these scaling factors as shown in equations 2.9, 2.10, and 2.11 below.

$$\bar{\omega} = \sqrt{\frac{A}{B}}\omega \quad (2.9)$$

$$F_{draw}^- = AC F_{draw} \quad (2.10)$$

$$\bar{D} = \frac{AC}{B^2}D \quad (2.11)$$

Then the non-dimensionalized scaling relationship for power and velocity can be rewritten using the above scaled factors in the form of a functional scaling law shown by equations 2.12 and 2.13.

$$v_{avg}(\omega, L, f, m, g, F_{draw}, \hat{\zeta}(\mu, \mu_w), D, \rho) = \frac{1}{\sqrt{AB}} v_{avg}\left(\sqrt{\frac{A}{B}}\omega, BL, f, Cm, Ag, CAF_{draw}, \hat{\zeta}(\mu, \mu_w), \frac{C}{B^2}D, \rho\right) \quad (2.12)$$

$$P_{avg}(\omega, L, f, m, g, F_{draw}, \hat{\zeta}(\mu, \mu_w), D, \rho) = \frac{1}{CA\sqrt{AB}} P_{avg}\left(\sqrt{\frac{A}{B}}\omega, BL, f, Cm, Ag, CAF_{draw}, \hat{\zeta}(\mu, \mu_w), \frac{C}{B^2}D, \rho\right) \quad (2.13)$$

This scaling law has powerful implications for modeling. Similar to how one can use the non-dimensional Reynolds number to make scale models of fluid flow, one could use this scaling law to model and test smaller scale tractors or cars, as opposed to testing on the life size vehicles. One could also use this scaling law to feasibly and cheaply test extraterrestrial wheel designs here on Earth.

Chapter 3

Physical Experiment Design

All of the above mentioned expansions to RFT were originally derived and tested using the MATLAB simulation. Following the initial validation of the above mentioned optimization techniques and functional scaling law experimental validation was required. The various processes used to design the four-spoke wheels, set up the physical tests, and analyze the data are detailed in the sections below.

3.1 3D Printing of Wheels

In order to conduct physical testing of the simulation carried out in MATLAB, first a physical representation of the simulated four-spoke wheel had to be created. A lab space and testing apparatus also needed to be found (lab space described in Section 3.2).

The first step in producing a physical version of the simulated four-spoke wheels was creating a SolidWorks model of the general four-spoke wheel design shown below. At first the method of coupling the four-spoke wheel to the motor was unclear so the initial design assume it would be press-fit onto the motor output shaft. Therefore the wheel's center consisted of a small cylinder with a hole through it that could be adjusted to the size of the motor's output shaft. The rest of the design was relatively simple consisting of exactly what had been simulated, a series of four identical spokes, each with a hinge halfway down each tread set to a prescribed angle θ . Figure 3-1 shows a rendering of the initial four-spoke wheel design.

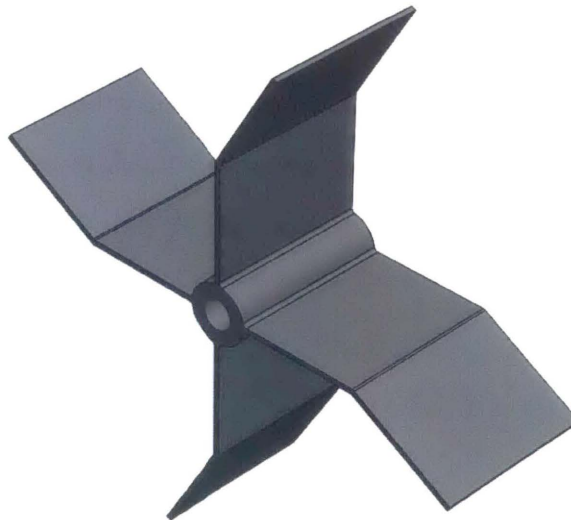


Figure 3-1: Initial four-spoke wheel design.

Following the identification of a lab space detailed in Section 3.2 below, it was established that the prior method of coupling wheels to the motor output shaft employed two cross-shaped pieces. The wheels they tested had hollow central hubs. One cross was placed on the outer face of the wheel and the other on the inner. The two crosses were fastened together using a set of four screws. In the middle of the two crosses, and the wheels as well, was a shaft hole. In the shaft hole of the outer cross was a cylindrical clamp that when screwed down fastened itself via friction to the mo-

tor output shaft. Figure 3-2 depicts the two cross shaped pieces and the cylindrical clamp.

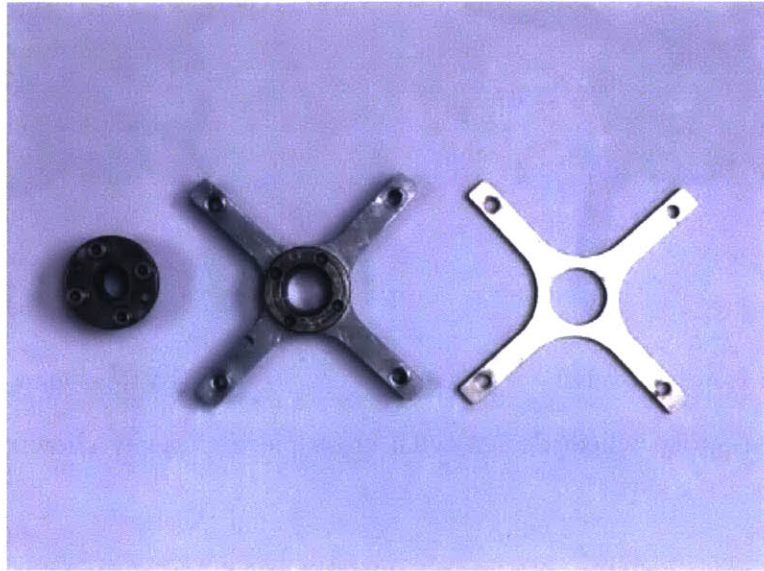


Figure 3-2: Cross pieces along with cylindrical clamp that together were used to couple four-spoke wheels to the motor output shaft.

Once this new method of coupling the wheel to the motor output shaft was discovered a corresponding change was made to the original design of the four-spoke wheel. The center shaft hole was expanded to become a hollow central hub. The profile of the cross-shaped piece was cut into both the inner and outer faces of the hub and the length of the tread connected to the central hub was reduced such that its effective length remained the same. A representative version of the updated four-spoke wheel design is shown in Figure 3-3 from two different perspectives.

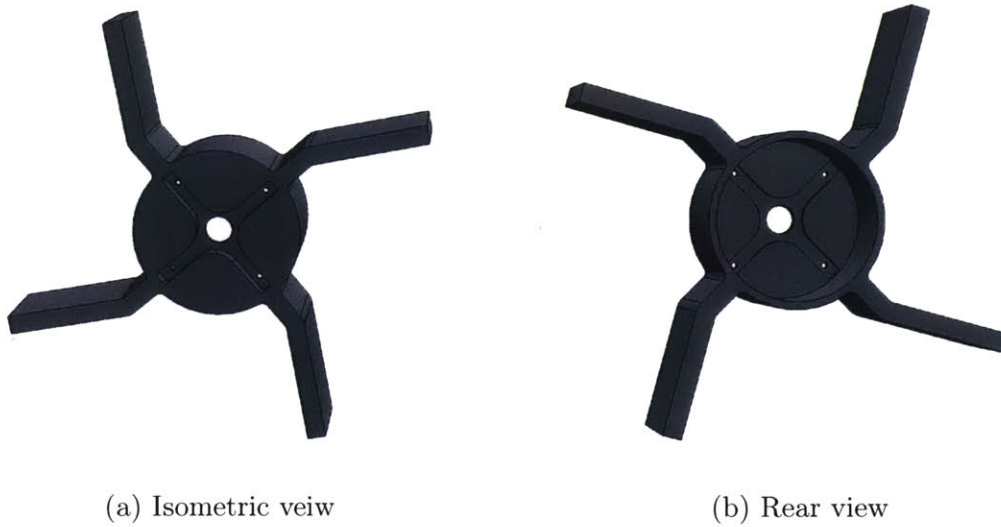


Figure 3-3: Four-spoke wheel design with cross piece cutaway shown from multiple perspectives.

After creating a SolidWorks model, a method of physically producing the model was needed. Several possibilities were considered including machining, molding, assembling from plastic or wood, or 3D printing. 3D printing was determined to be the fastest, cheapest, and most readily accessible way of producing the four-spoke wheel. Access to a Makerbot Replicator 2, desktop 3D printer was provided by Karl Iagnemma. This desktop printer had a relatively large build volume, 11.2 L x 6.0 W x 6.1 H in. The Replicator 2 was also a very fast 3D printer able to print all of the parts designed for the physical experiments in 12 hours or less. Figure 3-4 displays a Makerbot Replicator 2.

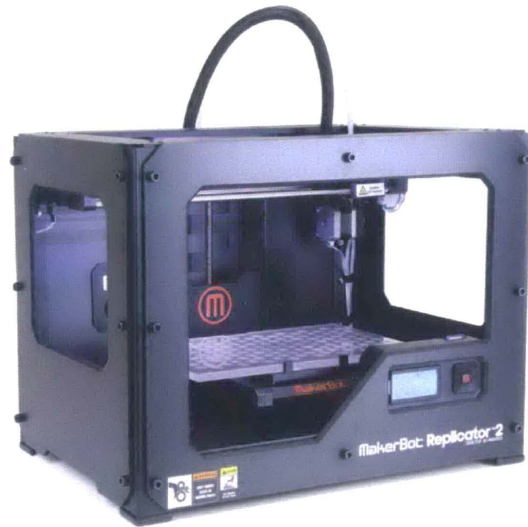


Figure 3-4: Makerbot Replicator 2 Desktop 3D Printer [1].

The last step in producing the four-spoke wheels was actually printing them. However, in an effort to print the wheels in the most efficient and effective manner several steps were optimized. First the decision had to be made as to the type of 3D printer material to use, either Polylactide (PLA) or ABS both thermoplastic polymers, had to be made. PLA was chosen to be the better material for the purposes of the physical experiments. It is more rigid and thus better able to hold form under load. Similar to ABS, it also can be machined and sanded allowing for post-printing processing of parts if necessary. PLA displays less part warping on a non-heated printing surface, which leads to more accurate parts, and the Replicator 2 does not offer a heated printing surface.

After choosing a type of material, support structures were added because the four-spoke central hub design featured excessive overhang angles. Lastly the part was chosen to have 10% fill, meaning only 10% of the infill, or internal volume of the part would be plastic. This internal plastic was printed in a honeycomb structure used to reduce the part weight, the consumption of printer material, and the print time per part. Then when it came time to print it was discovered that the wheel was too large to be printed in one piece. Thus it was cut in half, and printed in two symmetrical pieces. Fortunately the cross pieces attached on opposite faces of the central hub

proved to be a strong method of coupling the two pieces together. An example of a pair of four-spoke wheels used in testing is shown in Figure 3-5.



Figure 3-5: A pair of four-spoke wheels used in testing.

In addition to producing the plastic four-spoke wheel, a set of cylindrical wheels was also produced in order to test the validity of the functional scaling law. As such, one cylinder was a scaled version of the other. The cylinders, similar to the four-spoke wheel, were originally modeled in SolidWorks. They also were to be coupled to the motor output shaft using the cross pieces and thus had similar cross piece inlays. Lastly, once the cylinders had been 3D printed their exteriors were lined with sandpaper in order to increase their traction. In order to test the scaling law, a series of scaling constants were chosen, with $A = 1$, $B = 1.55$, and $C = 2.4$. These scaling constants were smaller due to experimental constraints. In order to generate a range of velocity and power outputs the two wheels were tested with a series of three unique vertical loads and three unique drawbar forces. Vertical loads of 41, 54, and 66.7N and drawbar forces in the range of -30N to 12N were applied to the small wheel. Scaled up vertical loads of 100, 130, and 160N and scaled up drawbar forces in the range of -50N to 30N were applied to the large wheel. The other inputs of the system are detailed in Table 3.1 below.

Table 3.1: Cylindrical Wheel Inputs [3]

Small Wheel Scale	Small Wheel	Large Wheel Scale	Large Wheel
ω	$30^\circ/sec$	$\sqrt{\frac{A}{B}}\omega$	$24.1^\circ/sec$
R	8.08 cm	BL	12.5 cm
f	$\chi = 1$	f	$\chi = 1$
g	$9.81m/s^2$	Ag	$9.81m/s^2$
D	15 cm	$\frac{C}{B^2}D$	15 cm

The two cylinders that were tested are shown below in Figure 3-6. The sand paper exterior is clearly visible on the smaller wheel on the right.

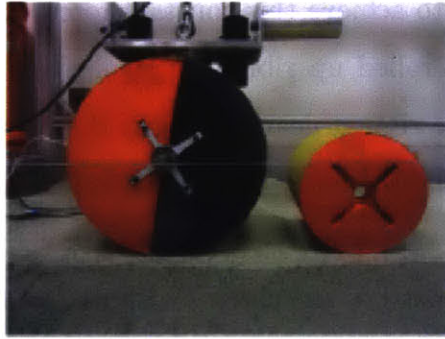


Figure 3-6: 3D printed cylindrical wheels.

3.2 Sand Test Bed Setup

In conjunction with designing and assembling the four-spoke wheels for testing, a location suitable to testing the wheels in conditions similar to those used in the MATLAB simulation as well as a testing apparatus were needed. Fortunately Karl Iagnemma allowed his lab space, the Robotic Mobility Group lab, to be used for the physical testing. The group had previously done work testing wheels for an extraterrestrial rover and had an experimental setup that was suitable for the physical experiments to be conducted.

The lab consisted of a sand bed contained in a transparent Lexan box with the test rig suspended above the sand. The wheels were attached to motor that was fixed

to a carriage that was free to move vertically via a set of bearings traveling along a pair of vertical rails. The carriage and the vertical rails along which it traveled was in turn connected a chassis that was free to move horizontally along a set of horizontal rails. Thus the entire system had three degrees of freedom, with the four-spoke wheel able to rotate along the motor axis, and the carriage free to move both horizontally and vertically along the two sets of rails.

There were two additional features of the rig that proved useful to the physical experiments conducted with the four-spoke wheels. First, there was a SDP/SI Neg'ator constant force spring, attached between the chassis and the carriage. Constant force springs do not obey Hooke's Law, as they exert a constant restoring force over their range of motion. In order to achieve this constant force, the Neg'ator constant force spring was composed of a rolled up ribbon of steel, fully relaxed in its fully rolled up state. The region of the ribbon near the roll is the primary driver of spring's the restoring force, and since the geometry of this region remains relatively constant, the spring's restoring force is approximately constant throughout the range of motion. The roll of the spring was fixed to the chassis with its free end attached to the motor carriage, and its purpose was to enable a reduction in the effective weight the carriage and motor when needed, as the two combined were quite heavy, weighing slightly more than 15lbs. The second feature of the rig was a pulley that was originally used to apply a drawbar force to the wheel, which effectively varied the direction of the gravity vector acting on the wheel. Figure 3-7 details the setup of the sand test bed and various forces acting on the wheel. $M_p g_e$ is the force due to the pulley, F_c is the force due to the constant force spring, $M_T g_e$ is the force due to the total mass of the wheel, and F_{res} is the resistive force of the sand.

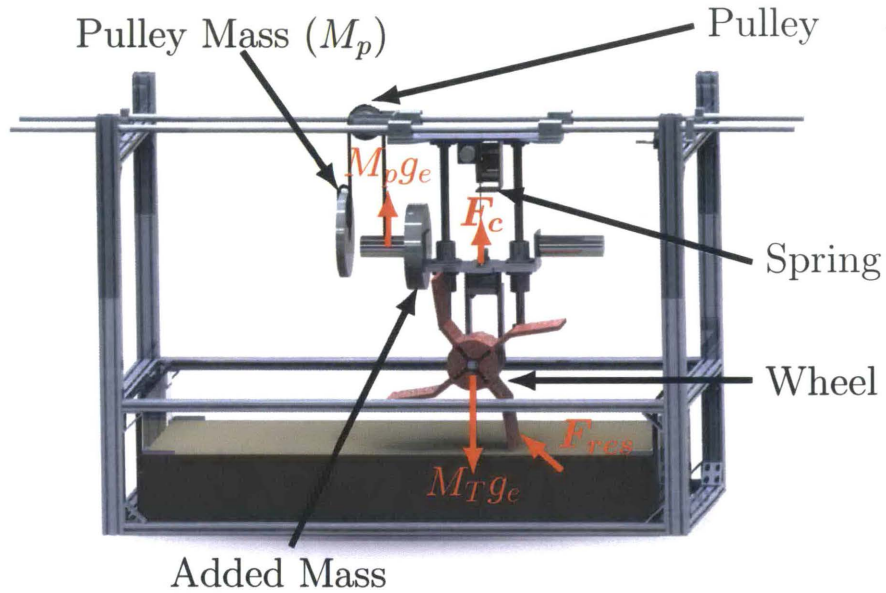


Figure 3-7: Sand test bed setup

It was discovered that the pulley, if used together with the constant force spring, could be used to vary the effective gravity acting on wheel. Note that in Figure 3-7 above the pulley is shown in the configuration used to vary effective gravity. This change in effective gravity can be derived by applying Newton's second law to the carriage as shown in equation 3.1.

$$\sum[F_y] = F_{res} + F_c + M_p g_e - M_T g_e = (M_T + M_p) \ddot{y} \quad (3.1)$$

Next the acceleration due to gravity is factored out from the pulley mass term, the wheel mass term, and the constant force spring term resulting in equation 3.2

$$F_{res} - (M_T - M_p - \frac{F_c}{g_e}) g_e = (M_T + M_p) \ddot{y} \quad (3.2)$$

Then the entire term multiplied by the acceleration due to gravity g is both multiplied and divided by a scaling factor k as shown in equation 3.3

$$F_{res} - \frac{(M_T - M_p - \frac{F_c}{g_e})}{k} kg_e = (M_T + M_p)\ddot{y} \quad (3.3)$$

Noting that for the following specific value of k ,

$$k = \frac{M_T - M_p - \frac{F_c}{g_e}}{M_T + M_p} \quad (3.4)$$

equation 3.3 becomes the following:

$$F_{res} - (M_T + M_p)kg_e = (M_T + M_p)\ddot{y} \quad (3.5)$$

The result is that equation 3.5 above describes a free wheel whose effective mass is $M_T + M_p$ and acceleration due to gravity is effectively kg_e . This effective gravity is shown in equation 3.6 below.

$$g_{eff} = kg_e = \frac{M_T g_e + M_p g_e - F_c}{M_T + M_p} \quad (3.6)$$

3.3 Data Collection and Analysis Methods

The goal of running the physical experiments was to gather data on the average steady state velocity and power expended and to compare it to the simulated results. Raw data about the forces and torques acting on the wheel were gathered through a three-axis force sensor, a three-axis torque sensor both attached to the motor carriage, and a torque sensor attached directly to the motor output shaft. The load cell for the force and torque sensors was positioned directly above the motor housing. The force sensor was thus able to accurately detect the effective mass of the wheel by measuring the net forces acting in the z-axis direction on the wheel, as well as determine the net drawback force experienced by the wheel. This data was then used to calibrate the physical experiments to have the same input values as the simulated experiments, namely that the effective wheel mass and drawback forces were identical. The torque

sensor was also positioned such that it could accurately detect the effective torque experienced by the wheel as it rotated, which was necessary to compute the power expended. There was an additional redundant torque sensor attached directly to the motor output shaft but was originally not used. Raw data on the position of the wheel was gathered via vertical and horizontal position sensors attached to the carriage. Lastly, an angular velocity sensor attached directly to the motor output shaft output data on the angular velocity of the wheel.

After collecting the raw data, a MATLAB script was used to process the data and compute the desired outputs of average steady state velocity and average steady state power expended. The entire code used for visualizing, processing and analyzing the raw data is available in Appendix A for reference. First a script was run in order to visualize all the raw data output from the various sensors through a series of graphs. A quick examination was then performed to make sure all sensors were outputting reasonable data. Then the start of the steady state was determined. First force and position data were analyzed to determine if the four-spoke wheel did in fact settle into an oscillatory steady state path with a constant period and amplitude in the confined length of the sand test bed. Steady state was to be identified by a relatively stable oscillations across a minimum of three periods in the z-axis force experienced by the wheel, whose oscillations were caused by the inertial forces arising from the wheel's four-spoke design. The steady state would then be confirmed by looking for similarly stable amplitude oscillations in the height of the four-spoke wheel's center of mass.

After a few rounds of testing, it was determined that if the wheel was simply set down on top the sand at the start of the test bed, which allowed for only four to five full rotations of the wheel from one end to the other, the sand bed was not long enough for the wheel to reach steady state. From data analysis it was determined that the wheels were continually digging themselves deeper into the sand throughout the four rotations, implying their steady state path required them to be further submerged into the sand. Thus in subsequent tests the wheels were started in a partially buried configuration, which placed them closer to their steady state position, to allow them

to reach said steady state in fewer rotations. In the tests following this change, the wheels were determined to reach sufficiently stable oscillations.

Once the oscillatory steady state was determined, the values of the average steady state velocity and power expended were calculated in MATLAB. In order to calculate the horizontal velocity, raw position data, gathered via the horizontal position sensor was processed using the MATLAB function "diff" to compute its derivative. However, the raw position data output from the sensor was somewhat noisy, meaning there were sometimes large jumps between the discrete data points output from the sensor, and taking its derivative exaggerated the noise. Therefore the MATLAB smoothing function "smooth" was applied to the angular position data to reduce the effects of noise. Then when the derivative of the angular position was taken, a usable horizontal velocity was computed. No processing was necessary for the raw torque and angular velocity data as those were output directly from the sensors and were smoother.

Next, data for horizontal velocity, angular velocity, and torque were plotted on the same graph. Then the average steady state values were computed by taking a simple average of the three outputs over a single arbitrarily chosen steady state period. The average steady state velocity is equal to the average horizontal velocity over the chosen steady state period. The average steady state power expended is equal to the multiple of the average angular velocity and the average torque both taken over the chosen steady state period.

Following several physical experiments, a large and consistent error between the experimental and simulated results indicated one of the assumptions may have been flawed. Large irregular jumps in torque were discovered from analyzing the torque data from the sensor above the motor housing. This erratic torque reading suggested that the interface between the rails and the bearings of the motor carriage, which had been assumed to be approximately frictionless, may actually have experienced a significant amount of friction that led to systematic errors between the experimental and simulated results. Subsequently, Silicone Spray Lubricant, a synthetic silicone-based lubricant, was applied to the rails between each set of tests, which succeeded in reducing the amount friction between the bearings and the rails, and the torque

output became much more stable which consequently minimized the systematic errors.

Chapter 4

FrankenWheel Design

Following the initial physical experiments validation of RFT, a more extensive set of physical experiments was conducted. These more robust experiments included a greater number of tests and more variation among the input parameters. Furthermore, the ability of the lab setup to allow for variations in the effective gravity mentioned in Section 3.2 above, enabled the physical experiments to be conducted which validated the expansion of the scaling law to include changes in ambient gravity. Results from these experiments can be found in James Slonaker et. al's paper *Geometrically general scaling relations for locomotion on granular beds* [4].

After the extensive testing, another consequence of the RFT simulation was explored. RFT predicts that as motion and loading conditions of the wheel change, a corresponding change in the shape of the wheel would lead to an improvement in the wheel's performance. Thus the design of a self-actuated wheel, nicknamed the FrankenWheel, capable of altering its shaped while in motion was explored. In order isolate the effect of the change of shape of the wheel, the actuated wheel had to satisfy two conditions. First it needed to only change shape in the in-plane dimension, which required a method of achieving anisotropic deformation. Then second it needed to be sufficiently rigid in all of its fixed configurations. Sufficiently rigid meant that the wheel must not exhibit significant deformation in shape while under load. The second condition proved difficult to achieve as the wheel had to be able to change its shape and then maintain the new shape all while in motion and thus under load. If these

two constraints were met, the goal then became to identify the simplest and easiest design to produce the FrankenWheel in the lab.

4.1 Superball Design

When first designing the FrankenWheel, the goal was for the wheel to be able to actuate through the "superball" family of shapes. The "superball" family of shapes was chosen because it would produce wheel shapes that appeared more functional than the previously tested four-spoke wheels. The "superball" geometry is, however, still only defined by a single shape parameter, χ , as shown in equation 4.1.

$$\left|\frac{x}{R}\right|^{2\chi} + \left|\frac{z}{R}\right|^{2\chi} = 1 \quad (4.1)$$

Thus this family of shapes includes both circles and squares. When $\chi = 0.5$ the equation yields a square, and when $\chi = 1.0$ the equation yields a circle. When χ is between 0.5 and 1 the sides of the square balloon outward, and as χ decreases below 0.5, the sides of the square become concave like an inverted diamond. Lastly, as $\chi \rightarrow \infty$ the equation yields a larger square. Figure 4-1 shows the plots of the equation with different values of χ .

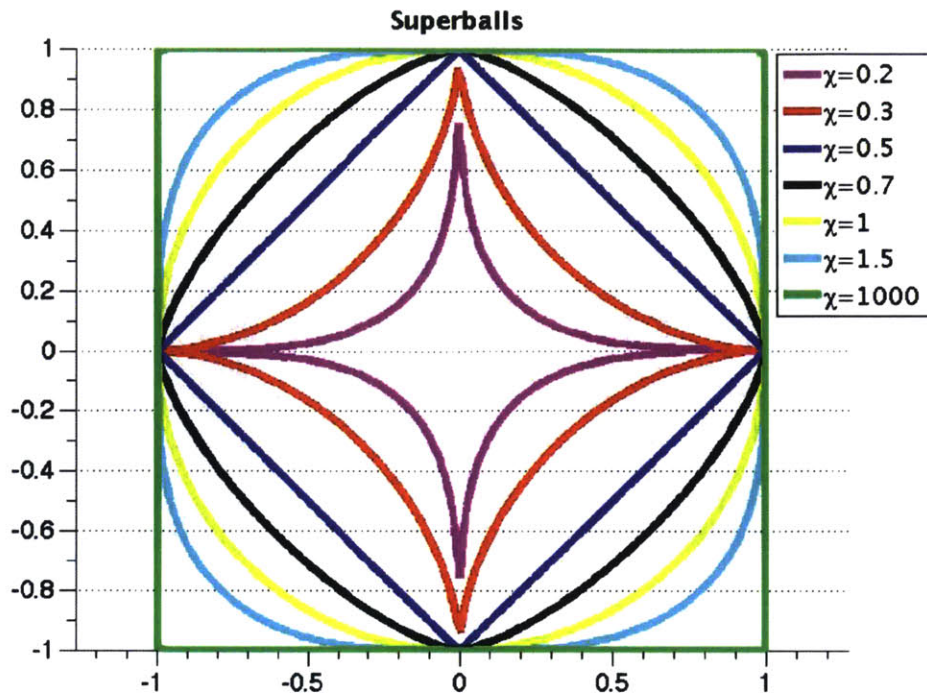


Figure 4-1: "Superball" shapes for different χ values.

It was determined that for the purposes of this experiment, the shapes should be confined to fitting within the same wheel well, as it is known that holding all else constant increasing the effective size of a wheel will lead to better performance. Therefore the FrankenWheel needed only be able to actuate between χ values of 0.3 and 1.

4.1.1 Design and Actuation

Utilizing the above constraints, design decisions could begin to be made. In order to achieve a shape profile that was smooth in both the concave and convex positions, a pressurized system appeared to be the best method of actuation, and relative to other fluids like water, air was determined to be the least messy and cheapest to acquire. Thus an air-pressurized system able to inflate and deflate membranes was explored. A plastic or metallic skeleton was proposed as a method to provide a rigid base to

which one could attach the membranes. In order for the wheel to meet the above constraints the rigid skeleton would have to have a profile of the smallest desired shape, i.e. its profile would be defined by $\chi = 0.3$. An early rendering of the skeleton of such a design is shown in Figure 4-2 below.

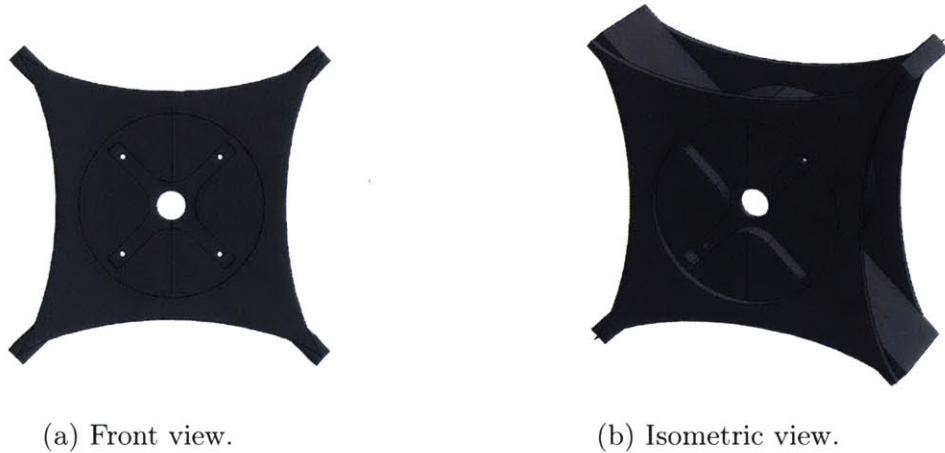


Figure 4-2: Multiple views of rigid skeleton design for the superbball shape family.

A membrane would encapsulate the skeleton and when negative pressure was applied to the system the membrane would shrink down to conform to the shape of the skeleton and when positive pressure was applied it would continuously expand outward, with the profile of the system progressing through the various values of χ . However several challenges with making such a design became readily apparent. One of which was that pressure is isotropic and thus when a negative pressure was applied the membrane would tend to sink into the empty space between the two inverted diamonds structures, and when positive pressure was applied the membrane would expand outward like a balloon. These extra deformations would violate the condition that deformation occurs in plane only. Another challenge was determining how to fix the membrane to the front and back faces of the rigid skeleton and how to prevent it from tearing at its corners were identified. Lastly determining a method to construct such an irregularly shaped membrane would definitely be a serious challenge.

In order to mitigate these challenges, several changes were made, but the idea of using a rigid skeleton was continued. First, it was determined that the range of shapes

could be further limited and still produce meaningful results. As such the range χ values was reduced to the range of 0.5-1.0 including only the shape change from a square to a circle. With the shape starting at a square and transitioning to a circle, a square-shaped skeleton could be used. Also smaller membranes could be employed to actuate the change in shape thereby reducing the out-of-plane deformation. These smaller membranes would also be easier to produce. One could simply heat seal two sheets of plastic together.

Utilizing these modifications, three versions of the pressurized system were designed. The first was a four-bag design with a spring steel-rubber interface. This design consisted of a single pneumatic actuator at the center of the square with a splitter and four valves connecting the actuator to the four membranous bags on each side. The bottom of each bag was bonded to the surface of the square and was covered by a rubber membrane to which the top of the plastic bag was bonded. The rubber membrane above the bags was then bonded to a strip of spring steel on either side. The spring steel strips were then attached to a hinge at each corner of the square. The actuator would pressurize all four bags causing them to expand pushing the rubber outward. The pressurized bags were designed to have an octagonal base to promote unidirectional expansion. The design of this four-bag rubber-spring steel interface is shown in Figure 4-3.

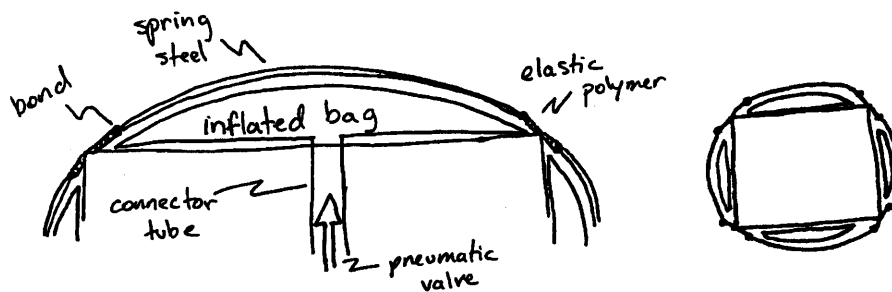


Figure 4-3: Drawing of four-bag rubber-spring steel interface design.

The second design was similar to the first and consisted of four membranous plastic bags sliding metal contact interface. The plastic bags were all still bonded to the surface of the square and still had octagonal bases. However, as opposed to

having a rubber membrane above them, there were thin metallic sheets. One sheet was attached to a hinge one side of the square and extended part way across the side, the other sheet was attached to a hinge on the other side of the square and extended far enough across the side so as to overlap with the opposite sheet. The two sheets were the connected by a sort of sliding clamp, either a C-clamp or a rolling contact, allowing the two sheets of metal to slide against one another as the plastic bag inflated below it. This sliding contact design is shown in Figure 4-4.

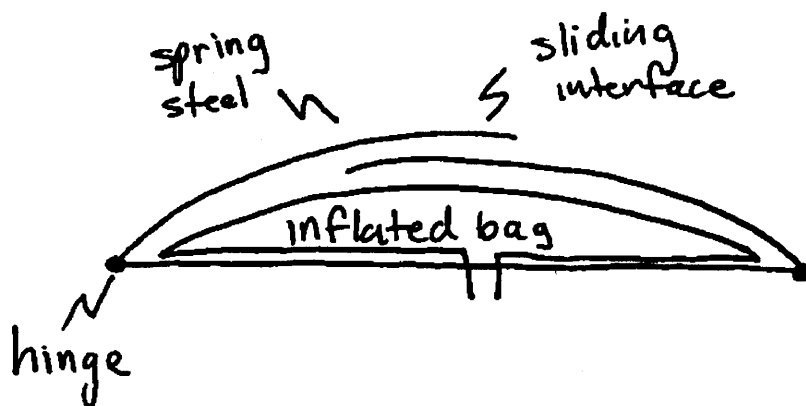


Figure 4-4: Sliding contact design.

The last design consisted of a single universal bag. A pneumatic actuator too would inflate this single plastic bag through a single connecting tube and valve. This design consisted of two square plates connected by four posts at each corner of the square. The bag was bonded to the inner surface of both faces and would consist of two circles and a ribbon of plastic heat sealed together to form a cylinder. The universal bag design is detailed in Figure 4-5.

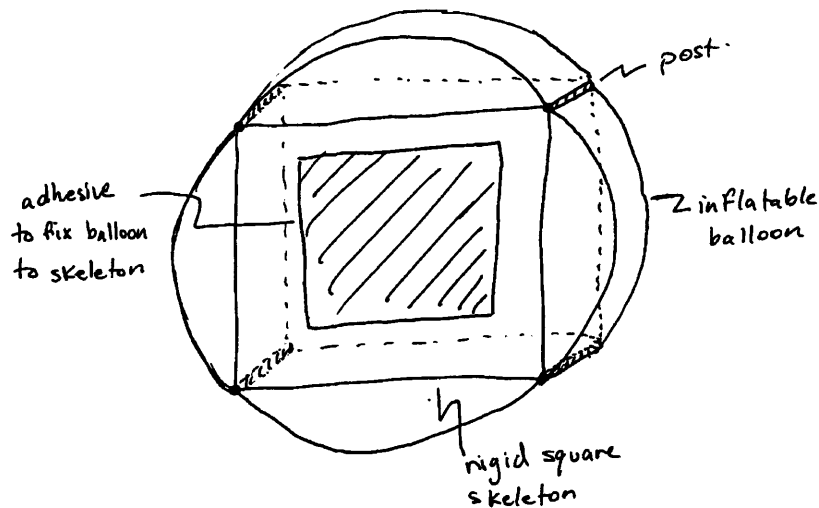


Figure 4-5: Universal bag design.

The universal bag design was quickly eliminated as it had very limited space for the pneumatic actuator relative to the other two designs, and the design could have strange effects due to the sharp points at the posts connecting the two faces. Next, the sliding metal contacts design was determined to be the better of the remaining two designs because it had fewer moving parts and would allow for the smoothest outer profile. However, further discussion revealed another challenge: with a single pneumatic actuator, which only regulates pressure, would inevitably cause significant deformation in the four inflatable bags. As wheel rotates only one bag is under load at a particular time, and with constant pressure that bag would compress while others expanded. Realizing this the idea for using air pressure to actuate, and subsequently the idea to actuate through "superball" family of shapes was scrapped.

4.2 FrankenWheel 2.0

With the original idea for the FrankenWheel to actuate through the "superball" family of shapes eliminated, it was back to the initial ideation phase. However, as had been discovered despite there being many different possible ways to realize the

end goal of designing a wheel that could change shape, many of them would require unnecessarily complex designs to achieve said goal. Thus the focus of the designs shifted toward simplicity in actuating a change in shape.

4.2.1 Ideation and Decisions

With the focus now on designs that could achieve the goal of in plane shape deformation, many different designs were considered such as a square with flanges, an actuated four-spoke wheel, and tank treads. The superball shape was even reconsidered. A list of the ideas that were generated each accompanied by a hand drawn depiction and its mode of actuation can be found in Figure 4-6 below.





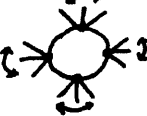
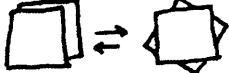
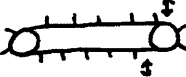
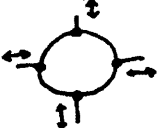
<u>Type</u>	<u>Drawing</u>	<u>Mode</u>
Super ball		Extension
4-Bar		Rotation
Square with Flanges		Rotation
Circle with Flanges		Rotation
Sun Wheel		Rotation
Rotating Square		Rotation
Tank Treads		Extension
Extended Protruder		Extension

Figure 4-6: Potential actuated wheel design ideas.

Next, to begin narrowing down the types of designs a Gantt chart was made to evaluate the designs at a high level on the basis of their mode of actuation. The mode of actuation was used as an initial distinguishing factor because the designs were split roughly in half into the two modes of actuation: rotation and extension. The categories chosen for evaluation were the following: knowledge, stability, and feasibility. The knowledge category was used to evaluate how well the method of actuation was understood. Stability indicated how strong the actuators were under

load. Feasibility was used a catchall to indicate how easy it would be to actually use the actuator. The Gantt chart is shown in Table 4.1.

Table 4.1: Gantt Chart of Rotation vs. Extension

	Rotation	Extension
Knowledge	0	-1
Stability	0	+1
Feasibility	0	-1
Total	0	-1

As shown in Table 4.1 above extension was not favored. Rotation was used as the baseline, and thus it received a score of zero in all categories. Extension was ranked better than rotation in terms of stability. All of the rotating designs featured a long lever arm that would directly amplify the torque that the actuator would have to overcome. However, extension was ranked worse in terms of both knowledge and feasibility. Extension ranked worse in terms of feasibility because it required a one to one ratio of actuators to moving parts, whereas with rotation there was a potential to reduce the number of actuators to one central part. Lastly extension ranked worse in terms of knowledge because linear actuators used for extension were less familiar than typical motors used for rotation. After choosing rotation as the mode of actuation, the various rotation-based designs were analyzed. It became clear that most were a variation of a single archetype: a central hub with rotating flaps along its exterior. With this realization, the flanged cylinder, the design that looked the most like a functional wheel, was chosen.

4.2.2 Actuation Method

The flanged cylinder originally consisted of a central hub and four moving flaps. The idea was that while the wheel was rotating a series or perhaps a single actuator would rotate the flaps to a specific angle relative to the hub making the flaps expand outward away from the center. A simplistic rendering of the flanged cylinder is shown in Figure 4-7.

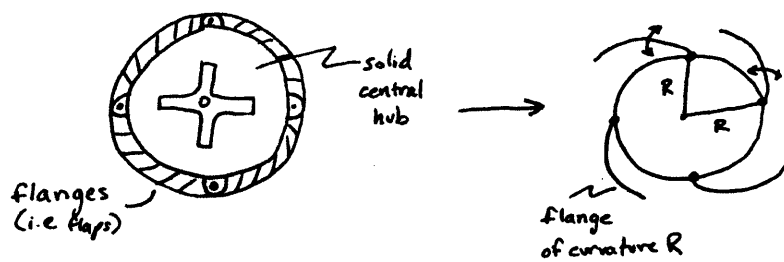


Figure 4-7: Four-flanged cylinder concept.

Four different design ideas were considered for actuation. The first design featured a single motor mounted in the center of the wheel hub paired with four strings each attached to the outer edge of one of the flaps. The motor would pull the string and rotate the flap away from the hub. This tension would resist the resistive force applied by the sand. However with this configuration, there would be nothing preventing the flap from rotating past its specified angle. As the wheel rotated, the flap would continue rotating under its own weight as the string attached to it only provided support in tension. Thus a spring or some device like it would need to connect the inner side of the flap to the outer side of the hub to prevent this unwanted motion. Figure 4-8 depicts the string-motor design.

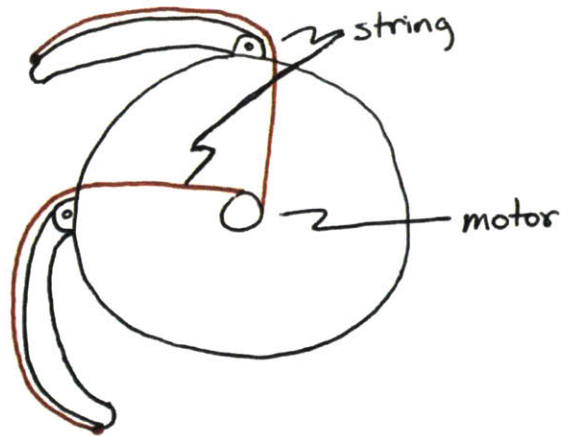


Figure 4-8: String-motor design.

The second design was similar to the first except that instead of four strings attached to the flaps, it consisted of four pulleys attached to the shafts around which the flaps rotated. If necessary a ratchet and paw could be connected to the shaft and hub, respectively, to help prevent counter rotation under load. Figure 4-9 depicts the pulley-motor design.

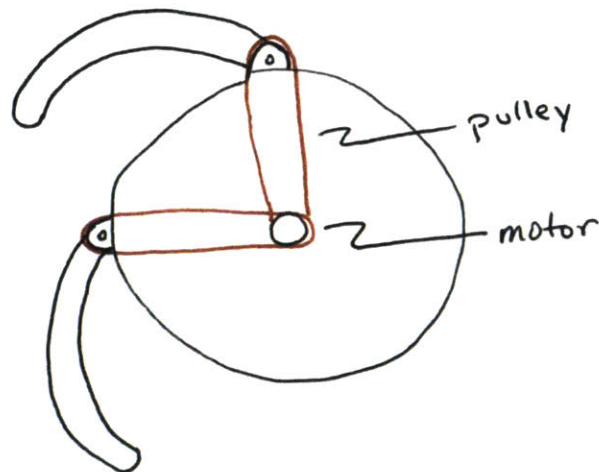


Figure 4-9: Pulley-motor design.

Despite eliminating extension as a method of actuation, it was revisited in the

third design, which was composed of a series four of pistons that would linearly actuate the flaps. In such a configuration the center of the wheel would be hollow and all the pistons would be mounted on the hubs exterior. Then in order to pair the rotation of the flap with the pistons linear actuation, the pistons would be mounted to the shaft of the next flap over, as shown in Figure 4-10.

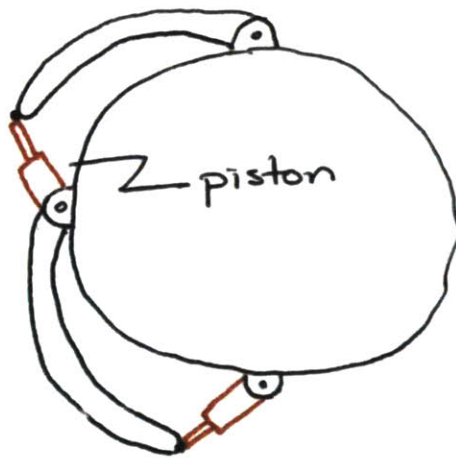


Figure 4-10: Piston actuated design.

Lastly, the fourth design was inspired by the original "superball" design of the FrankenWheel. It consisted of a series of pneumatically actuated balloons. A single balloon was located underneath each flap. They would be positioned near the tips of the flaps so as to increase the mechanical advantage of their lever arm relative to the shaft. A pneumatic compressor, as opposed to a motor, would be mounted in the center of the wheel hub, and a series of valves and tubes would connect the compressor to the balloons. Figure 4-11 depicts the pneumatically actuated balloon design.

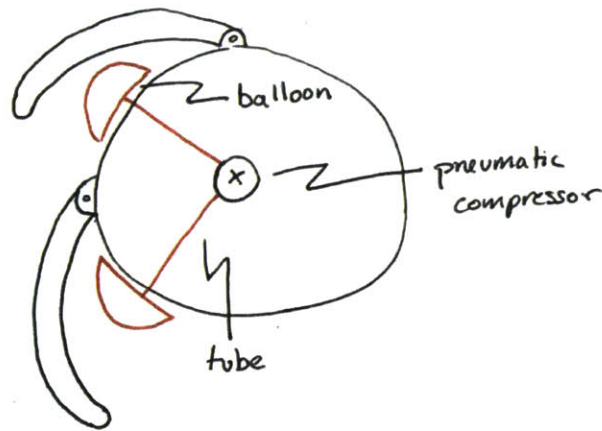


Figure 4-11: Pneumatically actuated balloon design.

The pulley design was chosen. It was more rigid than both the string-motor design and the pneumatically actuated balloon design. It also utilized a motor as opposed to the linear actuator featured in the piston design. However, the issue of slippage between the motor and the pulley remained, as well as the fact that in the pulley design would require four different pulleys to couple the motion of the motor shaft to that of the four flaps. In discussing how to reduce or eliminate these two issues, the idea to use a sprocket like in a bicycle gear chain arose. This subsequently sparked the idea to eliminate the sprocket-pulley system all together, by using a large central gear that was then coupled to a series of smaller gears attached to the shafts of the flaps. Such a system would reduce the number of moving parts and eliminate slippage between the motor and the pulley. A simple schematic of the new gear train design is shown in Figure 4-12.

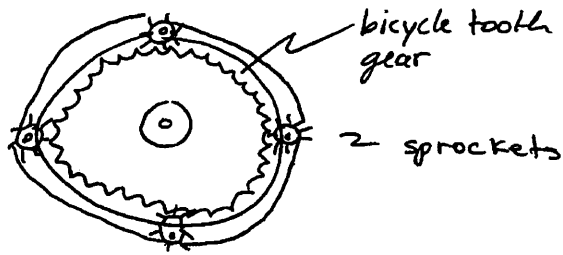


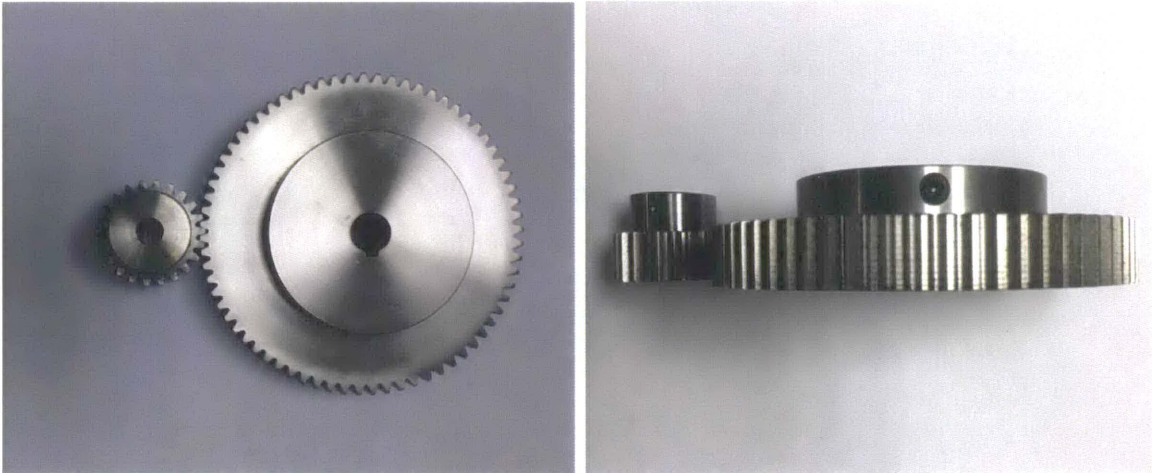
Figure 4-12: New gear train design.

Such a design required the central gear to be relatively large, as it had to have a radius comparable to that of the FrankenWheel. It also required the out gears to be small relative to the thickness of the flaps such that they did not protrude much into the sand as the wheel rotated. The small and large gears also needed to mesh, which meant they needed to have the same pressure angle and diametral pitch, if they were standard gears, or module, if they were metric gears. There are two standard pressure angles for gears, 14.5 degrees and 20 degrees. 20 degree pressure angle gears have a wider tooth profile than 14.5 degree gears and as such have greater strength to bear higher loads. Since the exact loading to be experienced by the FrankenWheel gears was uncertain, 20 degree pressure angle gears were used. Diametral pitch is a ratio defined for standard system gears as the number of gear teeth per inch of pitch diameter, meaning a gear with 16 teeth and a pitch diameter (PD) of 0.5in. would have a pitch equal to 32. Metric system gears however use modules but the ratio is similar, defined as the pitch diameter in millimeters divided by the number of teeth. Thus a gear with 16 teeth and a 32mm pitch diameter would be of module 2.

The physical setup, requiring a large central gear coupled with smaller outer gears, created a mechanical disadvantage reducing the effective gear ratio of the motor. In order to minimize this disadvantage and reduce the torque requirements for the motor, an outer gear radius of approximately 25mm was specified. Similarly, the large gear needed to be as small as possible, but it was limited in how small it could be. The FrankenWheel was to be attached to the drive shaft of the motor that would turn

the entire wheel via the same cross-shaped pieces that had attached the four-spoke wheels used in earlier testing. Thus the outer diameter of the large wheel had to be at least as large as that of the cross. Finally the large and small gears needed to be able to have suitable coupling methods to the motor output shaft and flap shafts, respectively. The coupling decision for the large gear was dependent on the type of gear head utilized with the motor, and as it turned out the output shaft of the gear head purchased for the experiment was keyed. Thus the large gear was chosen to have the corresponding keyway as well as a setscrew to ensure the reliable transmission of torque. The smaller gears only needed to couple to the flap shaft and since it was simpler to purchase a circular shaft as opposed to a keyed shaft, the smaller gears was chosen to couple to the shaft solely with a set screw. This decision was made knowing that if the set screw alone slipped on the shaft, the shaft could be filed down to a flat surface strengthening the coupling method.

After substantial searching, a set of gears of the same module, adequately sized PDs, and appropriate methods of coupling, were identified for purchase from Misumi USA. The smaller gears had a PD of 33mm and the larger gear had a PD of 105mm. Figure 4-13 shows the two types of gears. The keyway used in coupling the large gear to the motor output shaft can be seen in Figure 4-13a, and the two set screws used in coupling both large and small gears to their respective shafts can be seen in Figure 4-13b.



(a) Larger and smaller gear mating. (b) Top-down view of large and small gears.

Figure 4-13: Small and Large Gears.

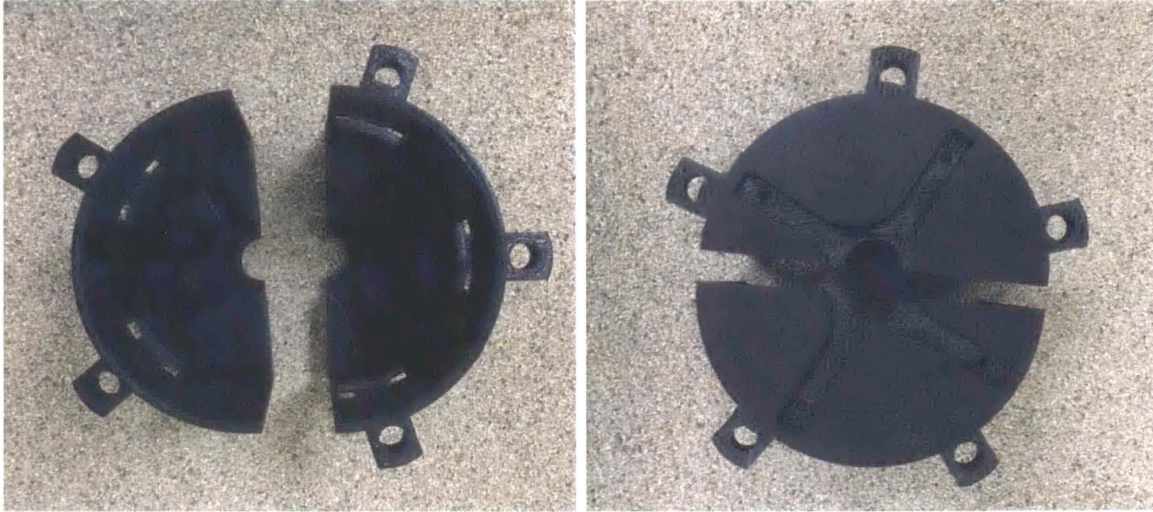
4.2.3 Central Hub and Flaps

Once the gears had been identified, the central hub and the flaps could be designed. The central hub was designed around the large and small gears. Its inner diameter needed to be large enough to fit the large gear. The central hub also had slots cut into it to allow the two gears to mesh, as the large gear was within the central hub and the smaller gears without. The hub also had a series of mounting features. It had posts with shaft holes along its exterior that would act as the bearings for the flaps' shafts. The hole for the shaft was positioned such that the smaller gear, which would be mounted to this shaft, was able to mesh with larger gear, meaning the pitch circles defined by the pitch diameters were tangent. Two holes were also positioned at opposite points of the central hub such that the motor mount itself could be mounted to the central hub. Figure 4-14 displays CAD images of the central hub.



Figure 4-14: SolidWorks image of central hub.

Lastly the central hub had the profile of the cross-shaped piece cut into its inner and outer faces. Then it was discovered that the central hub itself was too large to print in the Replicator 2 in a single piece. Therefore in order to print it, it had to be printed in two pieces, which would subsequently be held together by the cross-shaped pieces. The central hub has an inner diameter of 110mm, an outer diameter of 117.8mm thick, and is 100mm wide. Figure 4-15 displays actual photos of the two central hub pieces.



(a) Inside of central hub pieces.

(b) Front of central hub pieces.

Figure 4-15: 3D printed central hub.

Next, the flaps were designed to hug the contour of the outer diameter of the central hub. Thus the flap thickness was determined by the height of the shaft hole relative to the outer diameter of the central hub. A shaft hole was placed straight through one end of the flap allowing the shaft to pass through it. This part of the shaft ended in a semicircle to allow for its rotation relative to the central hub. The other end was curved such that it lay flat on top of the flap next to it. The flaps themselves were also designed with several recesses to accommodate the other moving parts. Each flap had two curved recesses that allowed the flap to rotate 90 degrees about the central hub's posts. Next there was a single recess at the top to allow for space for the small gear. Finally the curved end of the flap had another recess necessary to accommodate the small gear on its other side.

Originally the flaps were also designed to be coupled to the shaft using a device called Shaftloc, designed by SDP/SI to couple two rotating components. The single end version of Shaftloc was advertised to use an outer and an inner sleeve each with uniquely designed threads, which, when the inner sleeve was threaded into the inner sleeve, forced the outer sleeve to expand and the inner sleeve to contract fixing two rotating components together. The shaft holes on the outsides of the flap are larger

to accommodate the outer diameter of the Shaftloc device, while the inner shaft holes are only large enough for the shaft. The shaft size was chosen to be 8mm based on the availability of varying sizes of Shaftloc devices. In order for the flap to be able to withstand the force exerted on it by the Shaftloc devices and the torque from the wheel's weight and motor, they were chosen to be 10.1mm thick and their inner face have the same radius of curvature as the outer face of the central flap . Figure 4-16 below displays the design of the flaps, assuming Shaftloc would be used to couple the shaft and the flaps.



Figure 4-16: SolidWorks image of flap with Shaftloc coupling mechanism.

However, a contingency plan was also devised should the Shaftloc not work as advertised. A hole would be drilled through the flap and shaft and a set screw would be used to couple the two, coupling them. In the end the Shaftloc device unfortunately proved unable to couple the shaft to the flap, and this failure is discussed further in Section 4.2.5. Therefore the set screw method of coupling was used. The design of the flaps, assuming the set screw would be used to couple the flaps to the shaft, is shown in Figure 4-17.



(a) SolidWorks image of flap.



(b) 3D printed flap.

Figure 4-17: Flap design with set screw coupling mechanism.

Originally the FrankenWheel was going to have four flaps similar to the four spokes on the four-spoke wheels. However, in an attempt to reduce the effective load experienced by the motor and subsequently reduce the necessary torque required by the motor, it was decided that there would be five flaps on the FrankenWheel. Having five flaps, would reduce the effective torque born by each flap and could potentially reduce the maximum necessary torque required of the motor to open the flaps while the wheel was in motion.

4.2.4 Motor and Motor Mount

The actual specifications of the motor and the gear train were chosen independently based on the estimated conditions of the experiment. First the type of motor had to be specified; the choice was between brushed and brushless motors. Brushless motors were chosen because despite higher cost they required less maintenance, were more efficient, and had a higher power output to size ratio. Then the necessary torque limit for motor was determined by estimating the torque on the system when the wheel was stationary. This was calculated as the lightest effective weight of the wheel used in prior testing 20N multiplied by the effective length of the lever arm of

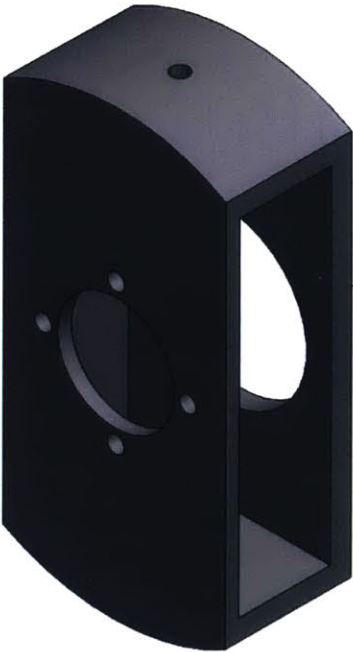
the flap 0.5m. Then this result was multiplied by a 2x safety factor resulting in an estimated system torque of 20Nm.

After choosing a type of motor and estimating the torque to be experienced by the system, the specifications of a motor and gear train could be determined. The motor and gear train combination needed to produce a maximum torque output of at least this 20Nm if not more. The maximum torque output of the combined motor and gear train is equal to the nominal continuous torque from motor multiplied by the gear ratio of the gear train. This maximum however needs to be below the max torque limit on the gear train or running the motor at its maximum continuous torque will break the gear head. Here it is worth noting that the small gears must only rotate a quarter of a full rotation to fully open the flaps. Therefore the gear ratio of the large gear to the smaller gears of approximately 1/3 (33mm/105mm) implies that the larger gear must only rotate 30 degrees to fully open the flaps. Due to said gear ratio, the motor did not need to rotate quickly at all in order for the flaps to open relatively quickly. As such speed was not a factor in choosing a motor.

With the above in mind, an EC 40 motor and a GP 42 C planetary gear head were selected for purchase from Maxon Precision Motors, Inc. The EC 40 motor had a maximum continuous torque of 165mNm. The GP 42 C has a gear ratio of 156:1 and a maximum torque limit of 22.5. Thus the maximum continuous operating torque would appear to be 24.92Nm as determined by the multiple of the max. continuous torque limit of the motor multiplied by the gear ratio. However, note that the maximum torque limit of the gear head is less than this, so the actual maximum continuous torque limit is 22.5Nm, which is still greater than the estimated system torque.

The overall design of the motor mount was created in tandem with the central hub and the flaps, with the specific design of components dependent on the type of motor used were postponed until the motor had been identified. The motor needed to be centered within wheel hub, and fixed to hub such that motor rotates relative to wheel itself. A potential problem with the motor being fixed relative to the wheel was identified. The wires attached to said motor would tangle as the wheel rotates.

However, the sand bed was determined to be short enough for this tangling to be insignificant over the course of a single test, but in order to untangle the wires, the wheel would need to be run in reverse between tests. With this problem addressed the motor mount was designed. The mount was hollow with holes to allow the planetary gear head to mount into with a set of screws. A large hole of diameter 42.1mm was placed into the back of the mount, such that the outer diameter of gear head housing would fit inside it. Then a second smaller hole of diameter 28.2mm with a series of set screw holes around it was placed into the front of the mount allowing the face of the gear head to mount into it. The two faces of the motor mount were spaced 22.7mm apart to allow for the gear head to be as close to simply supported as possible to reduce the torque experienced by the mounted face of the gear head. Holes were also placed in top and bottom of the motor mount allowing it to be fixed to central hub with another set of screws. Figure 4-18 depicts the motor mount.



(a) SolidWorks image of the motor mount.



(b) 3D printed motor mount.

Figure 4-18: Motor mount.

4.2.5 Production and Final Assembly

The central hub and the flaps of the FrankenWheel were printed using the same methods used for printing the four-spoke wheels detailed above in Section 3.1. The flaps were small enough to be printed with two flaps in each printing session. The central hub, however, was required to be printed in two pieces. The gears were stock parts ordered from Misumi USA. The motor and planetary gear head were also stock parts ordered from Maxon Precision Motors, Inc. A long single shaft was ordered from McMaster-Carr. Upon arrival a band saw was used to cut the shaft into five equal parts. Lastly, a set of single-end Shaftlocs were ordered from SDP/SI, and a set of screws were purchased from the shop in the Pappalardo lab. A SolidWorks image of the various components to be assembled for the FrankenWheel can be found in Figure 4-19 below. Only one flap, shaft, and small gear are shown for simplicity. From left to right the parts shown are the flap, the shaft, the small gear, the two pieces of the central hub, the large gear, the motor mount, and the combined planetary gearhead and motor. The cross pieces and other fasteners are not included in Figure 4-19.

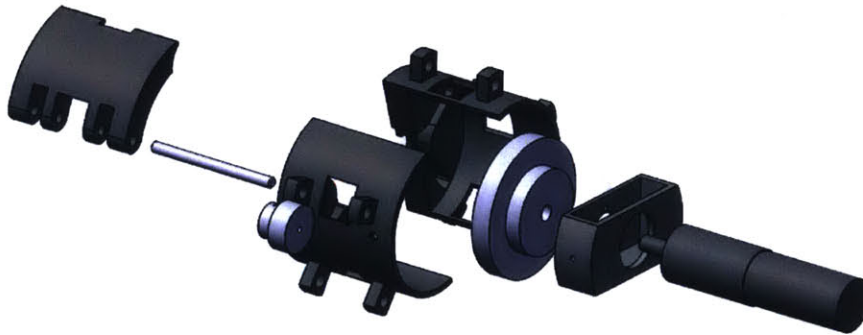
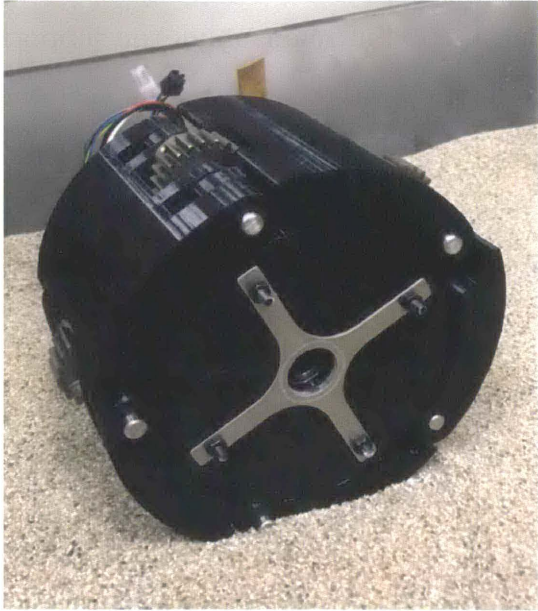


Figure 4-19: SolidWorks image of parts to be assembled for FrankenWheel.

In assembling the FrankenWheel, the shafts to be used with the flaps had to be filed down in order for them to fit into the bore diameter of the smaller gears. It was also discovered that the diameter of the shaft bore hole in the 3D printed parts which was the exact size of the shaft needed to be expanded as it was too small. The size of the bore hole was subsequently increased by 20%. The support material

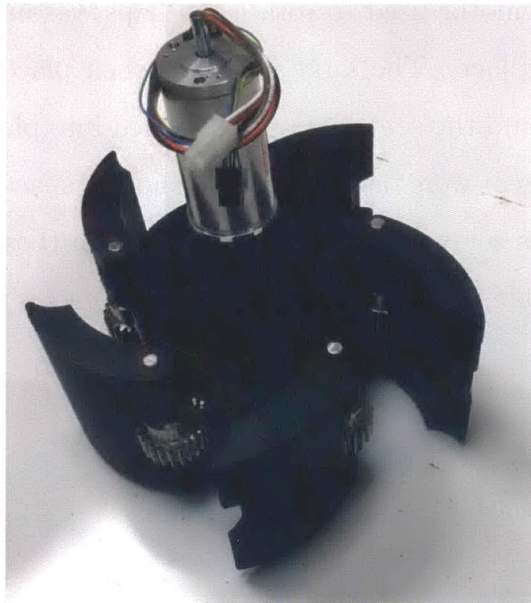
was removed from the 3D printed flaps and central hub but remnants of the support material had to be filed down in order for the flaps to rotate smoothly against the posts on the central hub. It was also discovered that the single-end Shaftlocs could not successfully mate the flap's shaft to the flaps and thus the roll pin method of coupling had to be used. The PLA material appeared to have too low of a coefficient of static friction to allow for a successful coupling. However, with these modifications in place the five smaller gears were placed into the slots on the flaps, then the flaps and gears were placed into position on the central hub. Next the shafts were inserted through the flaps, gears, and central hub. The screws were then screwed through the flaps and shafts securing the two together. Next the wheel was attached to the drive shaft of the motor that rotated the entire wheel using the cylindrical clamp of the cross-shaped pieces. The motor used to rotate the flaps was inserted into the motor mount and screwed into place. The large gear was then placed onto the planetary gear head's output shaft and the setscrew was tightened into place. Lastly, the motor mount, motor, and large gear were inserted into the hollow space of the FrankenWheel and the motor mount was screwed into position. With all these steps complete, the FrankenWheel was assembled. The assembled FrankenWheel is shown in Figure 4-20.



(a) Front of FrankenWheel.



(b) Rear of FrankenWheel.



(c) Isometric view of FrankenWheel.

Figure 4-20: Multiple views of the assembled FrankenWheel.

4.3 Further Experimentation

Opportunities to extend this research include physical experiments conducted with the FrankenWheel. In order for these to happen, several steps need to occur. First the motor used to rotate the flaps of the FrankenWheel needs to be connected to a

motor controller and a power source. A suitable motor controller has been identified. It is an EPOS2 70/10 motor controller and has been ordered from Maxon Precision Motors, Inc. A program to operate this controller and actuate the FrankenWheel, adjusting the flaps to the required positions, needs to be written either in LabView or on an Arduino. Following these steps a series of physical experiments needs to be conducted to validate the assumption that changing the wheel's shape does indeed improve the wheel's performance.

If the physical experiments validate these assumptions, then the next goal would be to create a truly "smart" tire that can sense its motion conditions and self-actuate to the optimal shape for those conditions. This will require some type of rapid feedback system likely involving data from the torque sensor on the motor and the load cell attached to the wheel. Using this data the FrankenWheel or another wheel like it could then sense for instance that its motion conditions had changed and it was stalling out in its current shape, by detecting its reduction in speed and increased power expenditure. Using the feedback system it could use this information to actuate a change in shape, thereby expanding its flaps to improve its performance, regaining speed and reducing power output.

Appendix A

Data Analysis Code

A.1 Data Visualization Code

```
1 % Matlab code to plot the information from the tests
2
3 %Clear everything
4 close all
5 clear all
6 clc
7
8 %folder = input('Which folder do you want to add to the path? ', 's')
9 %s = ['\' folder]
10 % P = path;
11 %path(P, s)
12 %Imports data from the raw sensor output
13 [b,a] = butter(5,0.01);
14 x = input('Which file do you want to read? ','s')
15 M = importdata(x, '');
16 t =     M.data(:,1);
17 d =     filtfilt(b,a,M.data(:,2));
18 v =     M.data(:,3);
19 tor =   M.data(:,4);
20 fx =    M.data(:,5);
```

```

21 fy = M.data(:,6);
22 fz = M.data(:,7);
23 tx = M.data(:,8);
24 ty = M.data(:,9);
25 tz = M.data(:,10);
26 sink = M.data(:,11);
27 angvel =M.data(:,12);
28 angvelp = M.data(:,13);
29 enc = M.data(:,14);
30 % lsen1 = M.data(:,14);
31 % lsen2 = M.data(:,15);
32
33
34
35 % The following command will plot several relevant measures
36 % against time.
37
38 %Displacement in the x-direction plot
39 figure(1);
40 hold on
41 plot(t,d)
42 xlabel('Time [s]')
43 ylabel('Displacement [mm]')
44
45 %Velocity plot
46 figure(2);
47 hold on
48 plot(t,v)
49 xlabel('Time [s]')
50 ylabel('Velocity [mm/s]')
51
52 %Torque from motor sensor plot
53 figure(3);
54 hold on
55 plot(t,tor,'b')
56 xlabel('Time [s]')

```

```

57 ylabel('Torque [Nm]')
58
59 %Three-axis force sensor output plot
60 figure(4);
61 hold on
62 plot(t,fx,t,fy,t,fz)
63 legend('Fx','Fy','Fz')
64 xlabel('Time [s]')
65 ylabel('Force [N]')
66
67 %Three-axis torque sensor output plot
68 figure(5);
69 hold on
70 plot(t,tx,t,ty,t,tz)
71 legend('Tx','Ty','Tz')
72 xlabel('Time [s]')
73 ylabel('Torque [Nm]')
74
75 %Displacement in the y-direction plot
76 figure(6);
77 hold on
78 plot(t,sink)
79 xlabel('Time [s]')
80 ylabel('Sinkage [mm]')
81
82 %Angular velocity of the wheel as output from the motor controller.
83 %This output is redundant as we used the angular position data
84 %output from the motor itself to compute the wheel's angular velocity.
85 % figure(7);
86 % hold on
87 % plot(t,angvel,'r')
88 % xlabel('Time [s]')
89 % ylabel('Wheel Angular Velocity [FROM MOTOR CONTROLLER]')
90
91 %Angular velocity plot. Calculated by taking derivative of the raw
92 %angular position data from the motor output shaft sensor.

```

```

93 wheel_angvel = diff(smooth(enc,10))/dt;
94 figure(9)
95 hold on
96 plot(t(1:end-1),wheel_angvel)
97 xlabel('Time [s]')
98 ylabel('Wheel Angular Velocity [deg/s]')
99
100
101 %Supplementary velocity computed to be used in calculating
102 %slippage below
103 dt = t(100)-t(99);
104 v = diff(d)/dt;
105
106 %Calculated slip plot. A measurement of how much the wheel
107 %turned in place throughout its motion.
108 figure(12)
109 hold on
110 t_start = 900;
111 plot(t(t_start:end-101),(1-(v(t_start:end-100)./(-wheel_angvel...
112 (t_start:end-100)*pi/180*(250/2))))*100);
113 xlabel('Time [s]')
114 ylabel('Measured Slip [%]')
115
116 figure(2)
117 hold on
118 plot(t(1:end-1),v,'r')

```

A.2 Steady State Averages Calculation Code

```

1 close all
2 clear all
3 clc
4
5 % Matlab code to plot the information from the tests

```



```

6
7 %folder = input('Which folder do you want to add to the path? ', 's')
8 %s = ['\' folder]
9 % P = path;
10 %path(P, s)
11
12 [b,a] = butter(5,0.05);
13 %[b,a] = butter(1,0.99991);
14 x = input('Which file do you want to read? ','s');
15 stop = 0;
16 count = 1;
17 while stop == 0
18 S(count).filename = x;
19
20 M = importdata(x, ', ');
21 t = M.data(:,1);
22 d = M.data(:,2);
23 v = M.data(:,3);
24 tor = M.data(:,4); %filtfilt(b,a,M.data(:,4)); %
25 fx = filtfilt(b,a,M.data(:,5));
26 fy = filtfilt(b,a,M.data(:,6));
27 fz = filtfilt(b,a,M.data(:,7));
28 tx = M.data(:,8);
29 ty = M.data(:,9);
30 tz = M.data(:,10);
31 sink = M.data(:,11);
32 angvel = M.data(:,12);
33 angvelp = M.data(:,13);
34 enc = M.data(:,14);
35 dt = t(100)-t(99);
36 wheel_angvel = diff(smooth(enc,10))/dt;
37
38 tororig=tor;
39
40 scrsz = get(0,'ScreenSize');
41 figure('Position',[1 1 scrsz(3) scrsz(4)])

```

```

42 plot(t,fz,t,tor); %abs(fz)./max(abs(fz)),abs(tor)./max(abs(tor)) %t,abs
43 %(fy)./max(abs(fy)),,t,abs(sink)./max(abs(sink)),t,abs(fx)./max(abs(fx))
44 %,t,abs(v)./max(abs(v))
45 hold on
46
47 legend('Fx','Fz','Torque','Sink','Fy','Vel')
48
49 [t_select,y_0] = ginput(4);
50 t_select = fix(t_select/dt); %divide times by dt and round towards zero
51
52 basezero=mean(tor(t_select(1):t_select(2))) %Added by J Slonaker
53 tor=tor-basezero;
54
55 [b,a] = butter(5,0.05);
56 fz_smooth = filtfilt(b,a,fz);
57 dfz = diff(fz_smooth);
58 thresh = .5*std(dfz);
59 t_sink_0 = find((abs(dfz(t_select(2):end)))>thresh,1);
60 t_sink_0 = t_sink_0+t_select(2)-1;
61 plot(t(t_sink_0(end)),abs(fz(round(t_sink_0(end))))/max(abs(fz)),...
62 'or','markersize',...
63 4,'linewidth',3)
64 [t_select_2,y_0] = ginput(1);
65 t_select_2 = fix(t_select_2/dt);
66
67 if abs(t_select_2-t_sink_0(end)) > 500
68     sink_0 = sink(t_sink_0(end));
69 else
70     sink_0 = sink(t_select_2);
71 end
72
73 close all
74
75 avg_fz = mean(fz(t_select(1):t_select(2)));
76 avg_fy = mean(fy(t_select(1):t_select(2)));
77 avg_fx = mean(fx(t_select(1):t_select(2)));

```

```

78
79
80 figure(3);
81 hold on
82 plot(t,tor,'k')
83 xlabel('Time [s]')
84 ylabel('Torque [Nm]')
85
86 figure(4);
87 hold on
88 plot(t,fy-avg_fy,'r',t,fz-avg_fz,'--r')
89 legend('Fx','Fz')
90 xlabel('Time [s]')
91 ylabel('Force [N]')
92
93 figure(6);
94 hold on
95 plot(t(t_sink_0:end),sink(t_sink_0:end)-sink_0)
96 xlabel('Time [s]')
97 ylabel('Sinkage [mm]')
98
99
100
101 %%% AVERAGE VALUES %%%
102
103 avg_start = fix(t_select(3));
104 avg_end = fix(t_select(4));
105
106 fz_avg = round((mean(fz(avg_start:avg_end))-avg_fz)*100)/100
107 fy_avg = round((mean(fy(avg_start:avg_end))-avg_fy)*100)/100
108 fx_avg = round((mean(fx(avg_start:avg_end))-avg_fx)*100)/100
109 tor_avg = round(mean(tor(avg_start:avg_end))*100)/100
110 sink_avg = round(mean(sink(avg_start:avg_end)-sink_0)*100)/100
111 angvel_avg = round(mean(angvel(avg_start:avg_end))*100)/100
112 angvelp_avg = round(mean(angvelp(avg_start:avg_end))*100)/100
113 vel_average = round(mean(v(avg_start:avg_end))*100)/100 %

```

```

114 power_average = round(mean(tor(avg_start:avg_end).*wheel_angvel...
115 (avg_start:avg_end)*pi/180)*100)/100 %
116 wheel_angvel_avg = round(mean(wheel_angvel(avg_start:avg_end))*100)/100
117
118 output = [-fz_avg -fy_avg tor_avg sink_avg -angvel_avg angvelp_avg fx_avg...
119 abs(vel_average) power_average abs(wheel_angvel_avg)];
120
121 figure(7)
122 plot(t,tor,'b.',t(avg_start:avg_end),tor(avg_start:avg_end),'g.')
123
124
125 mat2clip(output)
126 count = count+1;
127 close all
128
129 x_old = x;
130 test_num = find(isstrprop(x, 'digit'));
131 test_num = test_num(find(test_num>12));
132 digits = str2num(x(test_num));
133 x = [x(1:min(test_num)-1) num2str(digits+1)];
134 disp(['Is this filename correct?' ' ' x]);
135 y = input(['-Enter- to continue' '\n' '---0--- to re analyze the...
136 same data' '\n' '---1--- to stop the program' '\n' '---2--- to...
137 input a filename' '\n'],'s');
138 y = str2num(y);
139 if prod(size(y)) ~= 0
140     switch y
141         case 0
142             x = x_old;
143         case 1
144             stop = 1;
145         case 2
146             x = input('Which file do you want to read? ','s');
147     end
148 end
149 end

```

Bibliography

- [1] Makerbot replicator 2, May 8 2016. <https://www.3dhubs.com/>.
- [2] Chen Li, Tingnan Zhang, and Daniel I Goldman. A terradynamics of legged locomotion on granular media. *Science*, 339(6126):1408–1412, 2013.
- [3] James Slonaker. Wheel design optimization for locomotion in granular beds using resistive force theory. Undergraduate thesis, Massachusetts Institute of Technology, Mechanical Engineering Department, May 8 2016.
- [4] James Slonaker, Carrington Motley, Carmine Senatore, Karl Iagnemma, and Ken Kamrin. Geometrically general scaling relations for locomotion on granular beds. *arXiv preprint arXiv:1604.02490*, 2016.